Effects of Enhanced Front Walker Cell on the Eastward Propagation of the MJO

GUOSEN CHEN

Earth System Modeling Center, Nanjing University of Information Science and Technology, Nanjing, China, and Department of Atmospheric Sciences and Atmosphere-Ocean Research Center, University of Hawai'i at Mānoa, Honolulu, Hawaii

BIN WANG

Department of Atmospheric Sciences and Atmosphere-Ocean Research Center, University of Hawai'i at Mānoa, Honolulu, Hawaii, and Earth System Modeling Center, Nanjing University of Information Science and Technology, Nanjing, China

ABSTRACT

Well-organized eastward propagation of the Madden–Julian oscillation (MJO) is found to be accompanied by the leading suppressed convection (LSC) over the Maritime Continent (MC) and the western Pacific (WP) when the MJO convection is in the Indian Ocean (IO). However, it remains unclear how the LSC influences the MJO and what causes the LSC. The present study shows that the LSC is a prevailing precursor for eastward propagation of the MJO across the MC. The LSC enhances the coupling of IO convection and the Walker cell to its east [front Walker cell (FWC)] by increasing the zonal heating gradient. The enhanced FWC strengthens the low-level easterly, which increases boundary layer (BL) convergence and promotes congestus convection to the east of the deep convection; the enhanced congestus convection preconditions the lower to middle atmosphere, which further promotes the transition from congestus to deep convection and leads to eastward propagation of the MJO. The MJO ceases eastward propagation once the FWC decouples from it. Further analysis reveals that LSC has two major origins: one comes from the eastward propagation of the preceding IO dry phase associated with the MJO, and the other develops concurrently with the IO convection. In the latter case, the development of the LSC is brought about by a two-way interaction between the MJO's tropical heating and the associated tropical–extratropical teleconnection: the preceding IO suppressed convection induces a tropical–extratropical teleconnection, which evolves and forms an anomalous western North Pacific cyclone that generates upper-level convergence and induces significant LSC.

1. Introduction

The Madden–Julian oscillation (MJO) (Madden and Julian 1971, 1972) has attracted extensive attention in the meteorological society since the late 1980s, because it is the dominant component of tropical intraseasonal oscillation (ISO) and has significant impacts on the tropical and extratropical weather and climate (Madden and Julian 1994; Zhang 2005, 2013). Although having considerable advances after decades of endeavors, the simulations of the MJO in many GCMs remain problematic (Jiang et al. 2015; Ahn et al. 2017) and still have a lot of room for improvement (Neena et al. 2014; Lee et al. 2015). One of the major problems in the MJO simulations is that many present-day GCMs cannot simulate the eastward propagation of the MJO (Jiang et al. 2015; Wang and Lee 2017). This suggests that further improvement in our understanding of the MJO propagation mechanism is urgent and imperative.

The prototype of the MJO's propagation can be described as follows (Wang and Rui 1990b): the MJO's convection is initiated and enhanced in the Indian Ocean (IO), it propagates eastward and weakens while passing through the Maritime Continent (MC), and it reintensifies upon reaching the western Pacific (WP) warm pool and dies out upon reaching the cold tongue in the central Pacific (CP). However, not every MJO event goes through the above process. Observational studies (Matthews 2008; Kim et al. 2014; Feng et al. 2015; Zhang and Ling 2017) have shown that there exist propagating and nonpropagating MJO events. The propagating MJO events resemble the prototype and the MJO's convection anomalies could reach the WP, while the convection anomalies in the nonpropagating MJO events are confined in the IO. The propagating and the nonpropagating phenomenon of the MJO imply different dynamics

Corresponding author: Guosen Chen, chenguos@hawaii.edu

playing in the MJO propagation and different impacts of the MJO events on the global weather. Thus, it is necessary to understand what causes these different propagation phenomena.

When the MJO's convection develops in the IO region, the leading suppressed convection (LSC) anomalies, manifested as positive outgoing longwave radiation (OLR) anomalies or negative precipitation anomalies, are often found over the MC and WP regions. Kim et al. (2014) showed that MJO events can be grouped into propagating and nonpropagating cases according to the LSC (whose strength is measured by the magnitude of positive OLR). The strong MC–WP LSC corresponds to the propagating MJO case, while the weak LSC corresponds to the nonpropagating MJO case. Additionally, the MC–WP LSC is not a prerequisite for whether the MJO can pass through the MC region. As shown by Feng et al. (2015), the eastward propagation of the MJO across the MC can occur without the MC–WP LSC. However, their study indicates that the propagating MJO cases with stronger MC–WP dry anomalies have better eastward propagation (i.e., propagating farther east) than those with weaker MC–WP dry anomalies (shown in their Fig. 11). Their results (shown in their Fig. 10) also imply that most of the propagating MJO cases are accompanied by the MC–WP LSC. It is therefore suggested that the MC–WP LSC is important to eastward propagation of the MJO's IO convection.

Given the significance of the LSC, it is important to understand how it affects the eastward propagation of the MJO through the MC and what causes the LSC. In attempting to address the first question, Kim et al. (2014) showed that the eastward propagation of the MJO is driven by the column-integrated horizontal advection of moist static energy (MSE), which was dominated by the free-tropospheric meridional advection of mean MSE by the intraseasonal meridional wind anomalies that are interpreted as part of the LSC-induced low-level equatorial Rossby (ER) wave. They argued that this meridional advection by the ER wave moistens the atmosphere to the east of IO convection, thus promoting the eastward propagation of IO convection. However, Feng et al. (2015) showed that for the eastward-propagating MJO, the meridional moisture advection by intraseasonal wind anomalies does not depend on the strength of LSC. Additionally, Wang et al. (2017) suggested that the vertical advection of MSE by the second baroclinic vertical motion is more plausible for explaining the eastward propagation of the MJO. Thus, further studies are needed to understand through what processes the LSC affects the eastward propagation of the MJO. Another unaddressed question is what cases the LSC.

Although analyzing the vertically integrated MSE or moisture in the previous studies (Kim et al. 2014; Feng et al. 2015) is useful for understanding the MJO propagation, it ignores the vertically tilted thermal and dynamical structures of the MJO, and underestimates how these vertically tilted thermal and dynamical fields affect the eastward propagation of the MJO. For example, analysis of the column-integrated horizontal moisture convergence may underestimate the effects of leading boundary layer (BL) moisture convergence and the associated premoistening effects, processes that are known to be important to the MJO (Kiladis et al. 2005; Benedict and Randall 2007; Hsu and Li 2012; Wang and Lee 2017). In fact, the vertical structures of moisture and diabatic heating are found to be best correlated with the MJO propagation in a recent GCM study by Jiang et al. (2015), who showed that the rearward-tilted structures of moisture and diabatic heating are well simulated in the good models that are able to simulate the eastward propagation of the MJO from the IO to the WP, while no obvious vertical tilts are simulated in the poor ones. This implies that the premoistening, predestabilization, and lower-tropospheric congestus cloud heating induced by the BL moisture convergence are critical to the MJO's eastward propagation in good GCMs. However, the vertically integrated quantities may not detect these effects. Thus, it is suggested that the vertically tilted structures of the MJO and the associated zonal asymmetric structures (w.r.t. the MJO convection) should be emphasized in understanding of the MJO propagation (Wang and Lee 2017; Wang et al. 2018).

When the vertical structures of the MJO are considered, there are two Walker-like east–west cells associated with the MJO's major convection (Madden and Julian 1972): one is to the west of the MJO major convection and the other is to the east. We refer to the one located to the east as the front Walker cell (FWC) as it leads the MJO propagation. When there is LSC, the subsidence of the LSC constitutes the descending branch of the FWC. With a stronger LSC, the descending branch of the FWC will be stronger. Thus, it is argued by mass continuity that the FWC may be enhanced by intensified LSC. Since the eastward propagation of the MJO's convection is accompanied by the eastward propagation of the FWC (Madden and Julian 1972), the following question arises: can LSC affect the eastward propagation of the MJO through affecting the FWC?

Motivated by the above discussion, the major questions to be addressed in this study are how the LSC influences the MJO propagation and what causes the LSC. The first question concerns the mechanism by which LSC affects the MJO propagation. Addressing the second question has implications for forecasting the MJO

eastward propagation. The rest of this paper is organized as follows. Section 2 describes the datasets and methodology employed. The propagating and nonpropagating MJO events are selected in section 3. In section 4, the mechanisms of how the LSC affects the FWC and how the FWC affects the eastward propagation of the MJO are explored by analyzing the vertical tilted thermal and dynamical structures of the MJO. In section 5, the origins of the LSC are investigated. Section 6 presents the conclusions and discussion.

2. Data and methodology

a. Data

The primary data used in this study consist of the four times daily, 2.5° longitude × 2.5° latitude horizontal resolution ERA-Interim dataset (Dee et al. 2011) for the 34-yr period from 1979 to 2013. The horizontal and vertical wind components, geopotential height, and specific humidity are used in this study, and the daily mean is calculated from the four times daily records. We select 19 vertical levels from 1000 to 100 hPa with 50-hPa intervals. Daily averages of OLR data on a 2.5° square grid, sourced from the NOAA/NCEP interpolated OLR dataset, are used as a proxy for large-scale convective activity over the tropical regions (Liebmann and Smith 1996). In this study, we focus on the MJO events in the boreal winter from November to April (NDJFMA).

b. Methods

To extract the intraseasonal signals, the data-filtering process that follows Kim et al. (2014) and Wang and Lee (2017) has been applied to the daily data. First, the time mean and the first three harmonics of the climatological seasonal cycle are removed from the daily field. Then a 20–70-day Lanczos bandpass filtering (Duchon 1979) is applied to the data.

The composite analysis is used in this study to investigate the features of different MJO groups. The Student's t test is used to test the statistical significance of the composited fields. The degrees of freedom of the one-sample t test is $n - 1$, while the degrees of freedom of the two-sample t test is $n_1 + n_2 - 2$. For the composited mean, a two-sided Student's t test is applied; for the differences of the composited mean, a one-sided Student's t test is applied.

c. Wave-activity flux

To study the propagation of the extratropical teleconnection, the wave-activity flux (WAF) defined by Takaya and Nakamura (2001) is adopted in this study. The WAF is calculated by using Eq. (38) of Takaya and Nakamura (2001). For simplification, only the stationary part of the
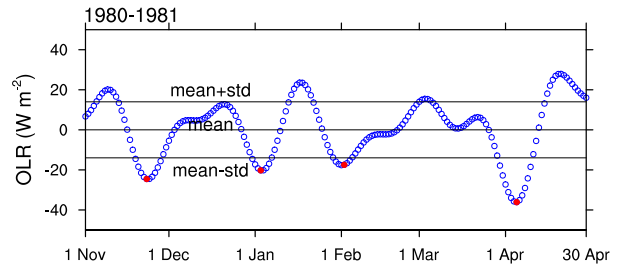

FIG. 1. Illustration of how the strong ISO event over the IO region is selected. Shown are time series of OLR index from November 1980 to April 1981 (blue hollow circles). The three horizontal lines indicate the mean OLR index (zero anomaly), the mean OLR index plus and minus one standard deviation. The reference date (with the lowest OLR index) of each strong ISO event is marked by a red filled circle. There are four selected events during this period.

WAF is calculated. Because of the low-frequency nature of the MJO and the associated teleconnection, this simplification is a reasonable approximation.

3. Classification of MJO events

From a practical (e.g., prediction) point of view, it is of great interest to ask whether a strong wet phase of ISO over the eastern Indian Ocean will propagate across the MC region, and whether one can find useful precursors that distinguishes propagating and nonpropagating cases. This invokes the ability to distinguish propagating MJO events from nonpropagating events. In this section, we describe how we classify the MJO events into the propagating and nonpropagating groups and how we further classify the propagating cases according to the LSC.

a. Selection of propagating and nonpropagating MJO events

The methods for identifying the propagating and nonpropagating MJO events are similar to those of Kim et al. (2014) and Feng et al. (2015). The first step is to identify ISO events that have strong convection over the IO region. To do this, we define an OLR index as area-averaged OLR anomalies over the IO region (10°S–10°N, 75°–95°E). The ISO event is then selected when the OLR index is lower than its mean minus one standard deviation for at least 5 successive days. For example, there are four selected ISO events during the period from November 1980 to April 1981, as shown in Fig. 1. We define the day with the lowest OLR index as a reference date of each multiday event. The reference dates for the four events shown in Fig. 1 are marked by filled red circles. There are 103 selected events during the 34 years.

To study the propagation mechanism of the MJO, the second step is to classify the selected events according to

their propagation features. Since the MC region is a barrier for the eastward propagation of the MJO (Zhang and Ling 2017), the selected events can be classified into the propagating and nonpropagating groups depending on whether they can pass through the MC region. Motivated by Feng et al. (2015), the propagating and nonpropagating MJO cases are selected in the following way. First, the Hovmöller diagram for each selected event is plotted. Then the propagating MJO cases are selected if the OLR contour of $-8\,\mathrm{W\,m^{-2}}$ can propagate eastward continuously and pass 125°E without any interruption. The nonpropagating MJO cases are selected if the propagation of convection (OLR equal to and lower than $-8\,\mathrm{W\,m^{-2}}$) stops before 125°E. There are 50 selected propagating cases and 43 selected nonpropagating cases. The nonpropagating (NP) cases here represent a group of strong ISO events occurring in the IO without farther eastward propagation, and they often show quasi-standing oscillation features, which will be shown later. The unselected cases are those in which the propagation of convection has interruptions or breaks. The classification of propagating and nonpropagating MJO cases here is consistent with Zhang and Ling (2017), who showed that about half of the MJO events forming over the IO can pass through the MC.

b. Further classification of propagating MJO cases

By examining the Hovmöller diagram it is found that the propagating MJO cases can be primarily classified into two groups according to the LSC. In the first group, the propagation of enhanced convection (or convective anomalies) from the IO to the WP closely follows the propagation of previous suppressed convection (or dry anomalies) from the IO to the WP. We refer to this group as the successive propagating (SP) cases, because it seems that the propagation of dry anomalies is succeeded by the propagation of convective anomalies. In another propagating group, the convective anomalies over the IO are not preceded by the propagation of dry anomalies but accompanied by a nearly simultaneous occurrence of dry anomalies over the MC–WP region (OLR anomalies on the Hovmöller diagram exceed $8\,\mathrm{W\,m^{-2}}$ and persist for over 5 days). Since the eastward propagation of convective anomalies is not preceded by the eastward propagation of dry anomalies, the second propagating group is referred to as the primary propagating (PP) with LSC cases. This terminology to some extent follows Matthews (2008). There are total of 50 propagating cases, among them are 23 SP cases and 21 PP with LSC cases. The rest of the cases (6 cases) are propagating cases without LSC.

Although the existence of simultaneous LSC over the MC–WP region is not a prerequisite for the eastward

propagation of the MJO, it is a common feature for those MJO cases that can propagate through the MC. In fact, the total number of the propagating cases with LSC (the SP and the PP with LSC) is 44, which accounts for 88% of the propagating cases. Thus, it implies that the LSC is a prevailing precursor for the eastward propagation of the MJO. For this reason, we focus on studying the roles of LSC in the MJO's propagation through the MC, and focus on the features of the SP, the PP with LSC, and the NP cases.

Figure 2 compares the general propagation features of OLR anomalies among the SP, the PP with LSC, and the NP cases. An interesting feature is that stronger LSC corresponds to farther eastward propagation of the MJO's convection. The SP case has the strongest LSC, and its convection signal ($-8\,\mathrm{W\,m^{-2}}$ contour of OLR) can reach the CP region (beyond 180°). The PP with LSC case has the moderate LSC, and its convection signal stops before 160°E. The NP case has no significant LSC, and its convection signal stops before 120°E. These features suggest the importance of the LSC to the eastward propagation of the MJO's IO convection. Note that the NP cases exhibit quasi-standing oscillation features, which is consistent with Kim et al. (2014).

The LSC associated with the propagating cases (the SP and the PP with LSC) exhibits variability of forms in their locations, intensities, timing, and origins. It is noted that the LSC in the SP cases is a part of the preceding dry phase of MJO event (Fig. 2a), while the LSC in PP with LSC cases does not appear to be a part of the MJO event (Fig. 2b). Figure 3 shows time–longitude evolutions of OLR anomalies from November 2002 to April 2003. During this period, there are three selected events: one SP event, one PP with LSC event, and one NP event. It is shown that the LSC in the PP with LSC event develops independently over the MC–WP region, indicating that the LSC is not necessarily a part of the MJO. Moreover, by examining Fig. 3, it is suggested that no matter whether the LSC is a part of the MJO or not, its generation over the MC–WP region can be regarded as a precursor for the eastward propagation of the MJO's convection. For this reason, we will also try to understand how the LSC occurs over the MC–WP without a preceding propagation of dry anomalies.

4. Mechanism by which the LSC affects the MJO eastward propagation

In this section, we explore how the LSC affects the eastward propagation of the MJO across the MC. We will demonstrate that the LSC can affect the coupling of the FWC to the MJO major convection, and the FWC can affect the eastward propagation of MJO convection.
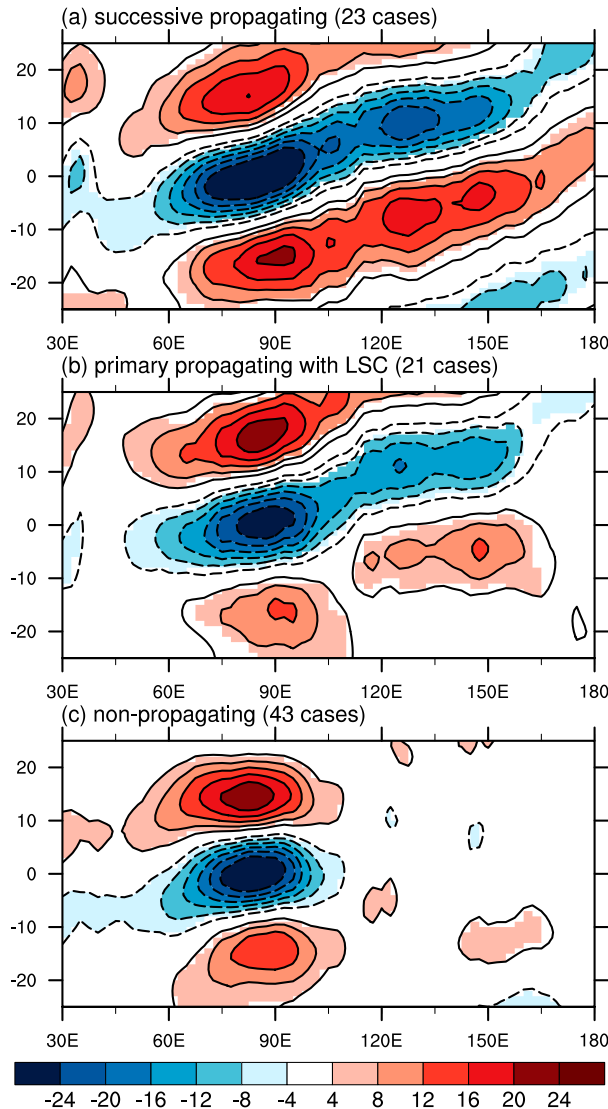
FIG. 2. Comparison of propagation features among the three MJO groups: composited longitude–time evolutions of OLR anomalies (W m^{-2}, contour) over tropics (10°S–10°N) for (a) the successive propagating (SP) cases, (b) the primary propagating (PP) with LSC cases, and (c) the nonpropagating (NP) cases. Day 0 represents the reference date of each MJO event used for the composite. The contour interval is 4 W m^{-2}. Those above the 95% confidence level are shaded.
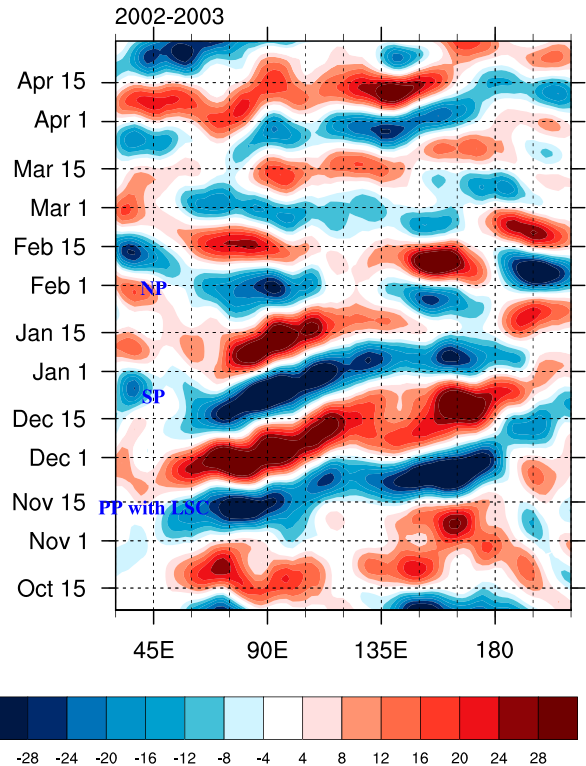

FIG. 3. Time–longitude variation of the intraseasonal OLR anomalies from October 2002 to April 2003. There are three se-lected events during this period: one SP event, one PP with LSC event, and one NP event, which are labeled.

a. The FWC as an indication of the eastward propagation

To understand how the LSC affects the eastward propagation of the MJO's convection, one needs to know what processes promote/impede the eastward propagation in the propagating/nonpropagating cases, and how these processes are related to the LSC. To answer these questions, the composited horizontal pat-terns of low-level circulation and OLR for the SP, the PP

with LSC, and the NP cases are compared (Fig. 4). In Fig. 4, P0 represents the zeroth pentad mean, of which the central date is the reference date of each event. $P - 1$ represents the pentad mean preceding P0, and so on.

The evolutions of OLR and low-level circulation for the SP cases (Fig. 4a) resemble that of the canonical MJO phase composites (Wheeler and Hendon 2004). There are clear convectively coupled Kelvin–Rossby wave structures from $P - 1$ to $P + 2$, with Kelvin wave to the east of the convection and Rossby wave to the west. For the PP with LSC cases (Fig. 4b), these convectively coupled Kelvin–Rossby structures are also evident from $P - 1$ to $P + 2$. Thus, the SP cases and the PP with LSC cases have common horizontal structures (i.e., the con-vectively coupled Kelvin–Rossby structures), even though the evolutions of suppressed convection are quite different in these two groups. Another common feature between these two MJO groups is that there are apparent suppressed convection anomalies over the MC–WP from $P - 1$ to P0, although the suppressed convection anomalies in the SP cases are stronger. These suppressed convection anomalies induce descending ER waves, which enhance the low-level easterly anomalies to the east of the IO convection in both cases.
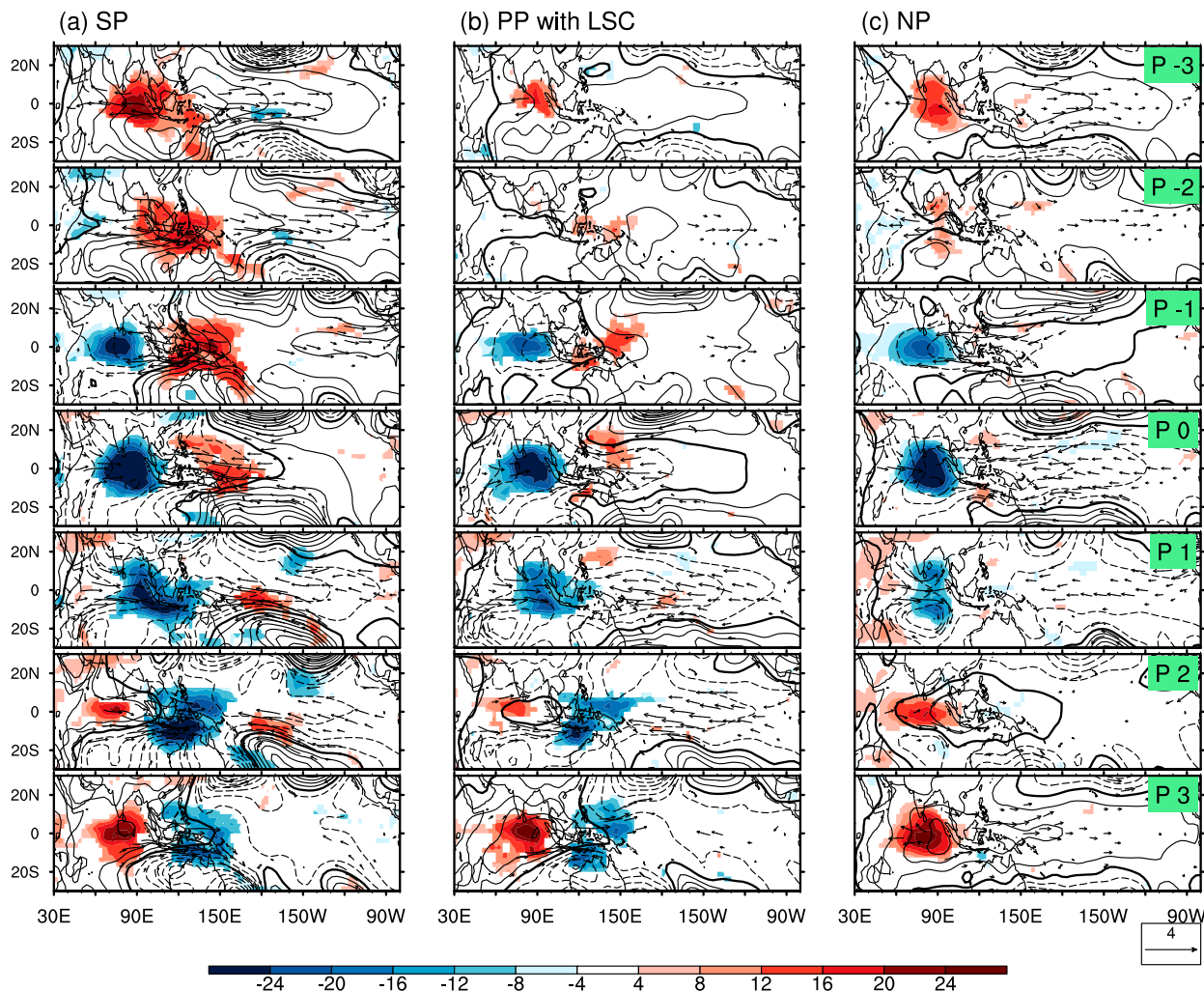
FIG. 4. Comparison of convection anomalies and low-level circulation anomalies among the three MJO groups: composites of OLR anomalies (W m^{-2}, shadings), 850-hPa geopotential height anomalies (m, contours), and the associated anomalous wind vectors (m s^{-1}, vectors) for (a) the SP cases, (b) the PP with LSC cases, and (c) the NP cases. The OLR anomalies and the wind vectors are shown for those above the 95% confidence level. The thin solid (dashed) contour indicates positive (negative) contour, and the thick solid contour indicates the zero contour. The contour interval is 2 m. P0 represents the pentad mean with central date being the reference date, $P - 1$ represents the pentad mean preceding the P0, and so on. A nine-point smoothing has been applied to the geopotential height field.

The evolutions of OLR and horizontal circulation in the NP cases (Fig. 4c) are different from those of the other two MJO groups. The convectively coupled Kelvin–Rossby structures are still observed from $P - 1$ to P0. However, the Kelvin wave propagates farther east on P0 compared to the other two MJO groups, suggesting a loose coupling of the Kelvin wave to the IO convection. The Kelvin wave decouples from the IO convection on $P + 1$. Accompanied with this decoupling of Kelvin wave, the precipitation pattern shifts poleward (on $P + 1$), indicating a transition from convectively coupled Kelvin–Rossby wave structure to convectively coupled Rossby wave structure. Without the coupling of Kelvin wave, there are no zonal easterly anomalies

coupled to the IO convection. Thus, the difference of low-level circulation between the propagating (the SP and the PP with LSC) and the nonpropagating cases is manifested by how well the low-level zonal easterly anomalies are coupled to the convection.

Since the low-level zonal easterly anomalies are part of the FWC, the coupling of low-level zonal easterly anomalies to the IO deep convection is equal to the coupling of the FWC to the IO deep convection. Figure 5 shows the vertical structures of circulation in the equatorial pressure–longitude section (vectors) and the vertical velocity along the equator (shadings). The common feature among the three MJO groups is that the ascending branches of the FWC are coupled with the
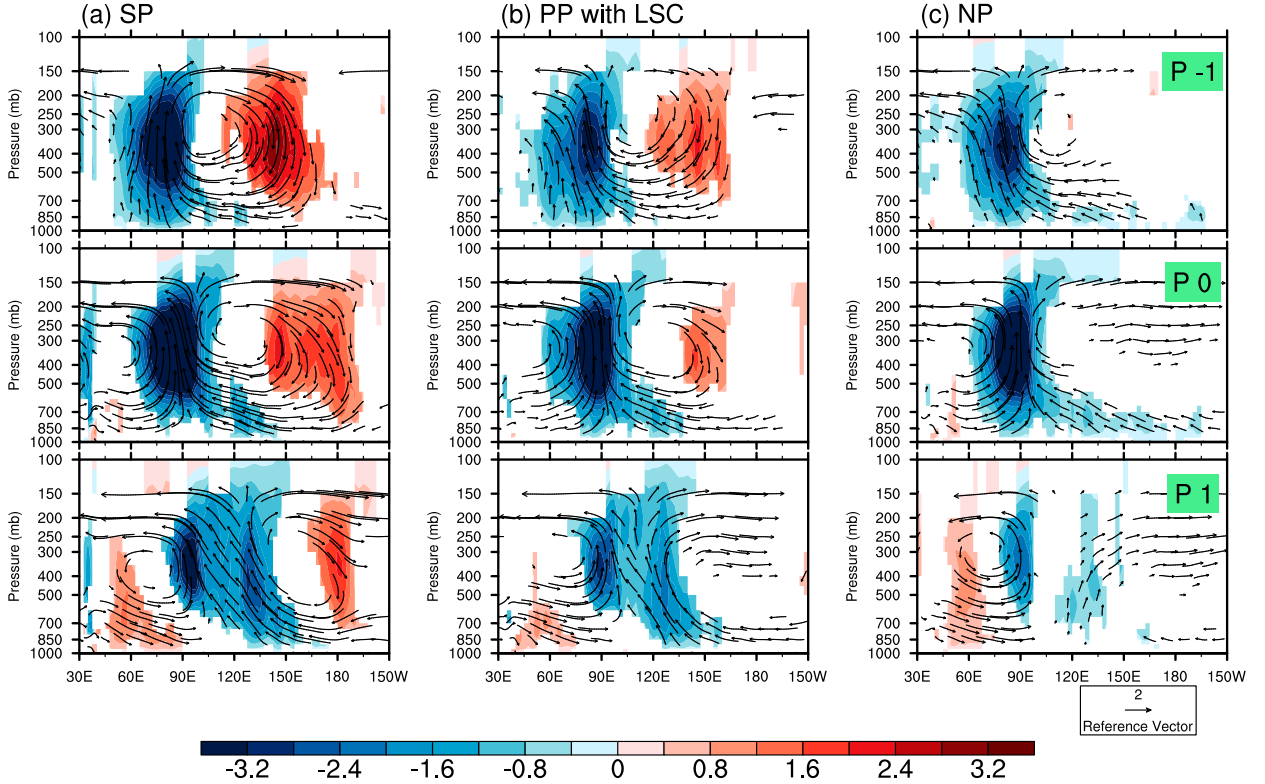
FIG. 5. Comparison of vertical structures of the FWC and the associated vertical velocity among the three MJO groups: composites of longitude–height structures of the equatorial vertical velocity anomalies (shadings, 0.01 Pa s^{-1}, averaged between 5°S and 5°N), and the anomalous wind vectors near the equator (vectors, averaged between 5°S and 5°N) for (a) the SP cases, (b) the PP with LSC cases, and (c) the NP cases. Only those above the 95% confidence level are shown. For the vectors, the vertical velocity anomalies are multiplied by a factor of −100.

IO deep convection. The differences come from the descending branches of the FWC. In the SP and the PP with LSC cases the descending motions of the FWC are associated with the LSC. There are closed FWCs in the SP cases (from $P − 1$ to $P + 1$) and the PP with LSC cases (from $P − 1$ to P0). In contrast, there are no significant descending branches of the FWC in the NP cases because of the lack of the LSC, and the FWCs are not closed. For the SP and the PP with LSC cases, the deep convection propagates eastward with its coupling to the FWC (from $P − 1$ to $P + 1$), while in the NP cases the deep convection ceases moving eastward once the FWC decouples from it (on $P + 1$). Therefore, it is suggested that the eastward propagation of the MJO is related to the FWC, and the coupling of the FWC to the MJO deep convection can be considered as an indication of the eastward propagation of the MJO.

b. How the LSC enhances the FWC

It is conjectured that the LSC can affect the FWC since the descending branch of the FWC is largely attributed to the subsidence induced by the LSC (Fig. 5).

To theoretically study the effect of the LSC on the FWC, we consider the nondimensional inviscid anelastic 2D equations for the first baroclinic mode of tropical motions (Kuang 2008a,b):

$$\varepsilon u = -\frac{\partial p}{\partial x}, \tag{1}$$

$$\varepsilon p + \frac{\partial u}{\partial x} = -Q, \tag{2}$$

where the circulation is considered as a stationary response to the convective heating Q. Here p and u are the low-level free atmospheric pressure and zonal wind, respectively, for the first baroclinic motion; and ε is the damping coefficient. This model resembles the Gill model (Gill 1980), except that it depicts the 2D motions in the longitude–height section in the tropics, especially the forced Walker cell.

Eliminating p in Eqs. (1)–(2), we have the following:

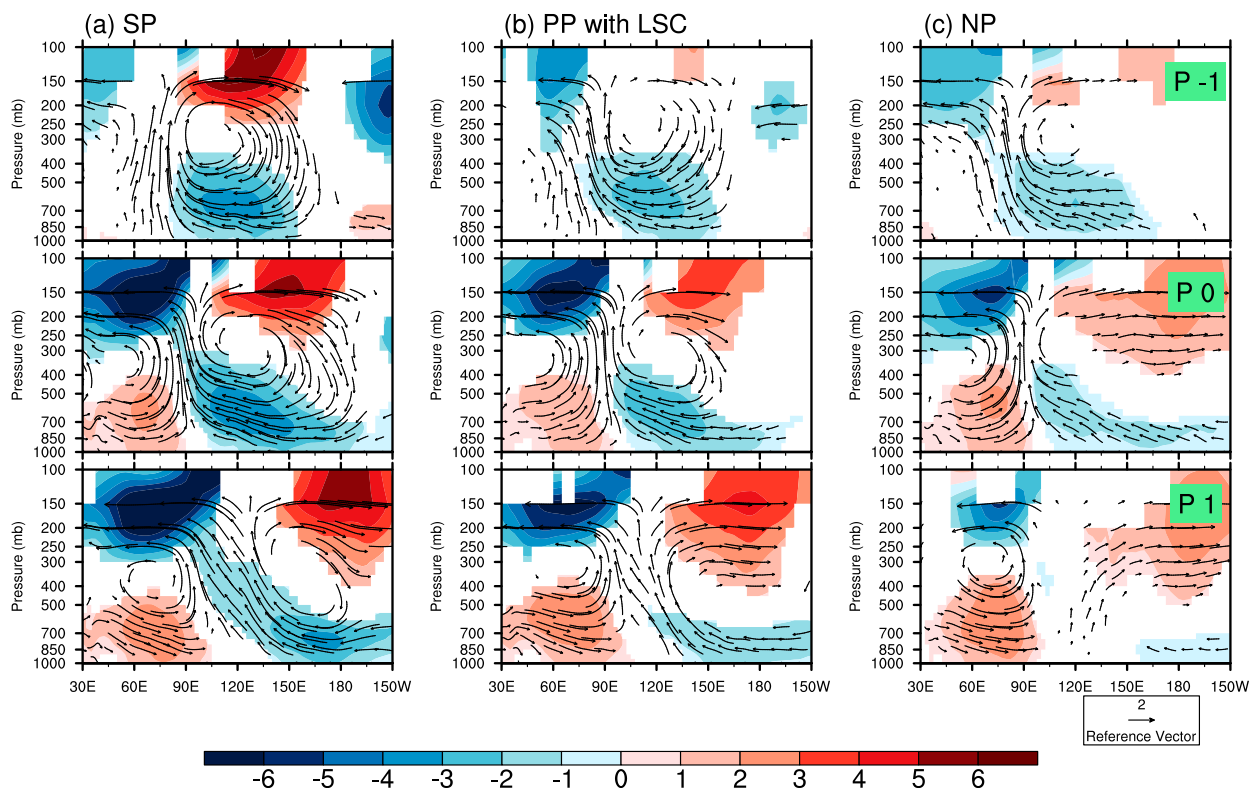$$\varepsilon^2 u - \frac{\partial^2 u}{\partial x^2} = \frac{\partial Q}{\partial x}. \tag{3}$$

FIG. 6. As in Fig. 5, but the shadings denote the zonal wind anomalies (m s^{-1}) averaged between 5°S and 5°N.

Since $\partial^2 u/\partial x^2 \sim -k^2 u$ when considering the wave solution (k is the wavenumber), Eq. (3) can be approximated by

$$(\varepsilon^2 + k^2)u \approx \frac{\partial Q}{\partial x}. \quad (4)$$

As indicated by Eq. (4), there will be low-level baroclinic easterly anomalies corresponding to a negative zonal heating gradient. Stronger zonal heating gradient leads to stronger low-level zonal easterly anomalies. According to the mass continuity equation, enhanced low-level zonal easterly anomalies could strengthen the ascending motion and the associated deep convection by providing intensified zonal convergence. This could in turn enhance the low-level zonal easterly anomalies, leading to enhanced FWC and its coupling to the deep convection. For a given IO heating strength, inclusion of LSC increases the amplitude of the zonal heating gradient. Therefore, the LSC could enhance the FWC and its coupling to the deep convection by increasing the zonal heating gradient.

The effect of the LSC on the FWC is manifested in Fig. 6. It shows that the strengths of the low-level zonal easterly anomalies are proportional to that of the descending motions. The SP cases have the strongest descending motions and the strongest low-level easterly anomalies, while the NP cases have the weakest descending motions and the weakest low-level easterly anomalies. This relation holds up from $P - 1$ to $P + 1$, supporting the relation indicated by Eq. (4). Additional evidence is that compared to $P - 1$, the low-level zonal easterly anomalies intensify in the SP and the PP with LSC cases on P0 in the presence of LSC, while they weaken in the NP cases on P0 in the absence of LSC. This implies that the LSC could enhance the FWC, which is consistent with the above theoretical analysis. In the SP and the PP with LSC cases, the enhanced FWCs are well coupled to the deep convection and these couplings persist through $P + 1$. Without LSC, the FWC in the NP cases weakens upon reaching the MC region on P0 and decouples from the deep convection on $P + 1$.

c. How the FWC affects the MJO eastward propagation

With the FWC being coupled to the deep convection, there are low-level zonal easterly anomalies to the east of the deep convection (Fig. 6). These zonal easterly anomalies are attributed to the Kelvin wave easterly anomalies and the ER wave easterly anomalies when the LSC is present, while they are solely attributed to the
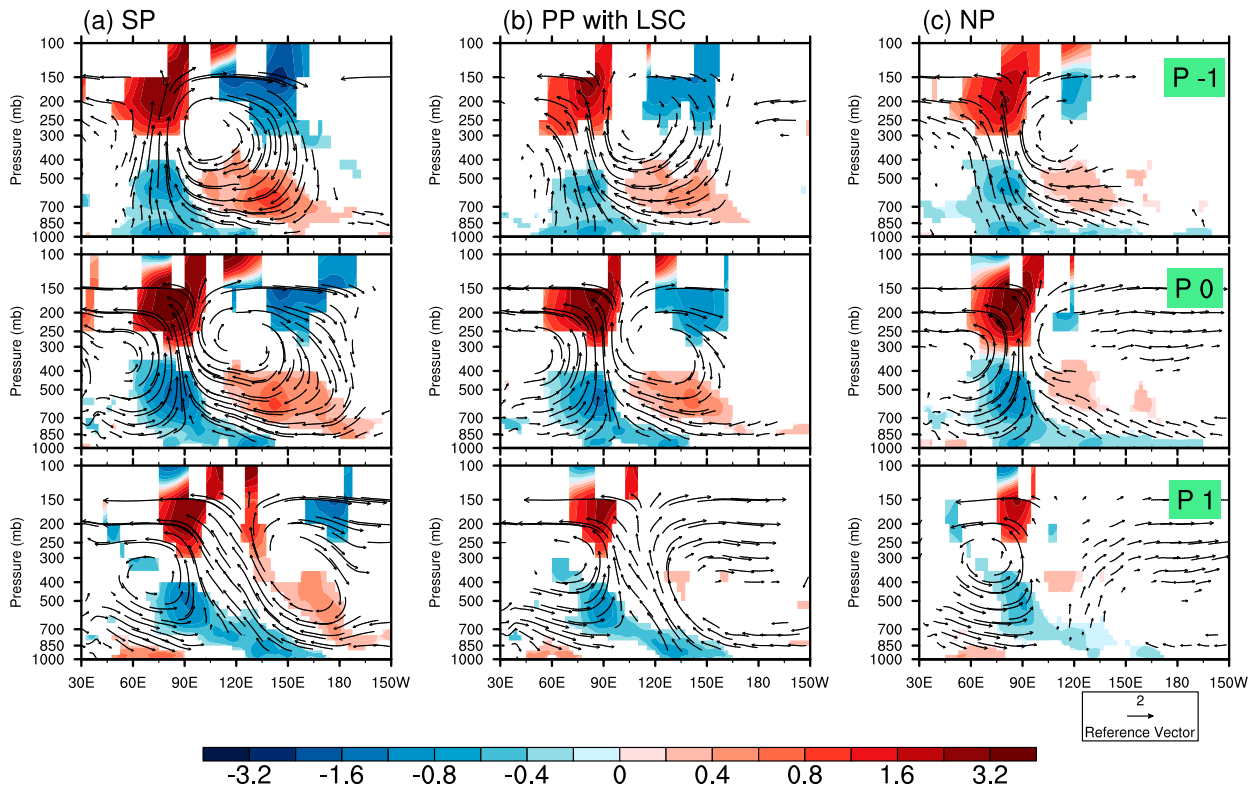
FIG. 7. As in Fig. 5, but the shadings denote the horizontal divergence anomalies ($1 \times 10^{-6}\,\mathrm{s}^{-1}$) averaged between 5°S and 5°N. A zonal five-point running average has been applied to the divergence field.

Kelvin wave easterly anomalies when the LSC is absent. Since both the low-level equatorial Kelvin wave easterly wind and the ER wave easterly wind correspond to the BL convergence near the equator (Wang and Rui 1990a; Wang and Li 1994), the coupling of the FWC to the deep convection suggests that there is leading equatorial BL convergence anomalies to the east of the deep convection.

Figure 7 shows the vertical structures of horizontal divergence for the three MJO groups. It shows that the leading BL convergence anomalies (1000–850 hPa, 105°–140°E) are developing on $P-1$ and developed on P0 in the three MJO groups. On P0, the SP and the PP with LSC cases have stronger BL convergence anomalies than the NP cases, which corresponds to the fact that the SP and the PP with LSC cases have stronger low-level zonal easterly anomalies than the NP cases (Fig. 6). The relation among the convection signals, the low-level zonal easterly anomalies and the BL convergence anomalies on P0 are further illustrated in Fig. 8. Corresponding to the differences in the LSC (Figs. 8a,b, 130°–170°E), the low-level zonal easterly anomalies (around 100°–150°E) in the SP and PP with LSC cases are significantly higher than those in the NP cases (Figs. 8c,d), which leads to stronger leading BL convergence (around 110°–140°E) in the SP and PP with LSC cases than the NP cases (Figs. 8e,f). The difference of the leading BL convergence between the SP and NP cases is significant around 120°–140°E, while the difference between the PP with LSC and NP cases is significant around 115°–125°E (Fig. 8f). As a result, Fig. 8 shows that the LSC can enhance the FWC and the low-level zonal easterly anomalies, which can further enhance the leading BL convergence.

The leading BL convergence anomalies propagate eastward with the FWC in the SP cases and the PP with LSC cases on $P+1$ (Fig. 7), while they dissipate quickly on $P+1$ in the NP cases once the FWC decouples from the IO convection. Therefore, the coupling of the FWC to the deep convection implies the existence of the leading BL convergence.

How does the leading BL convergence affect the eastward propagation of the MJO? The leading BL convergence can premoisten the lower atmosphere to the east of the deep convection (Hsu and Li 2012). As shown in Fig. 9, there are positive specific humidity anomalies accumulated at the lower atmosphere to the east of the IO convection (around 105°–140°E) on P0 in the three MJO groups. The premoistening of the lower atmosphere is well correlated with the leading BL convergence.
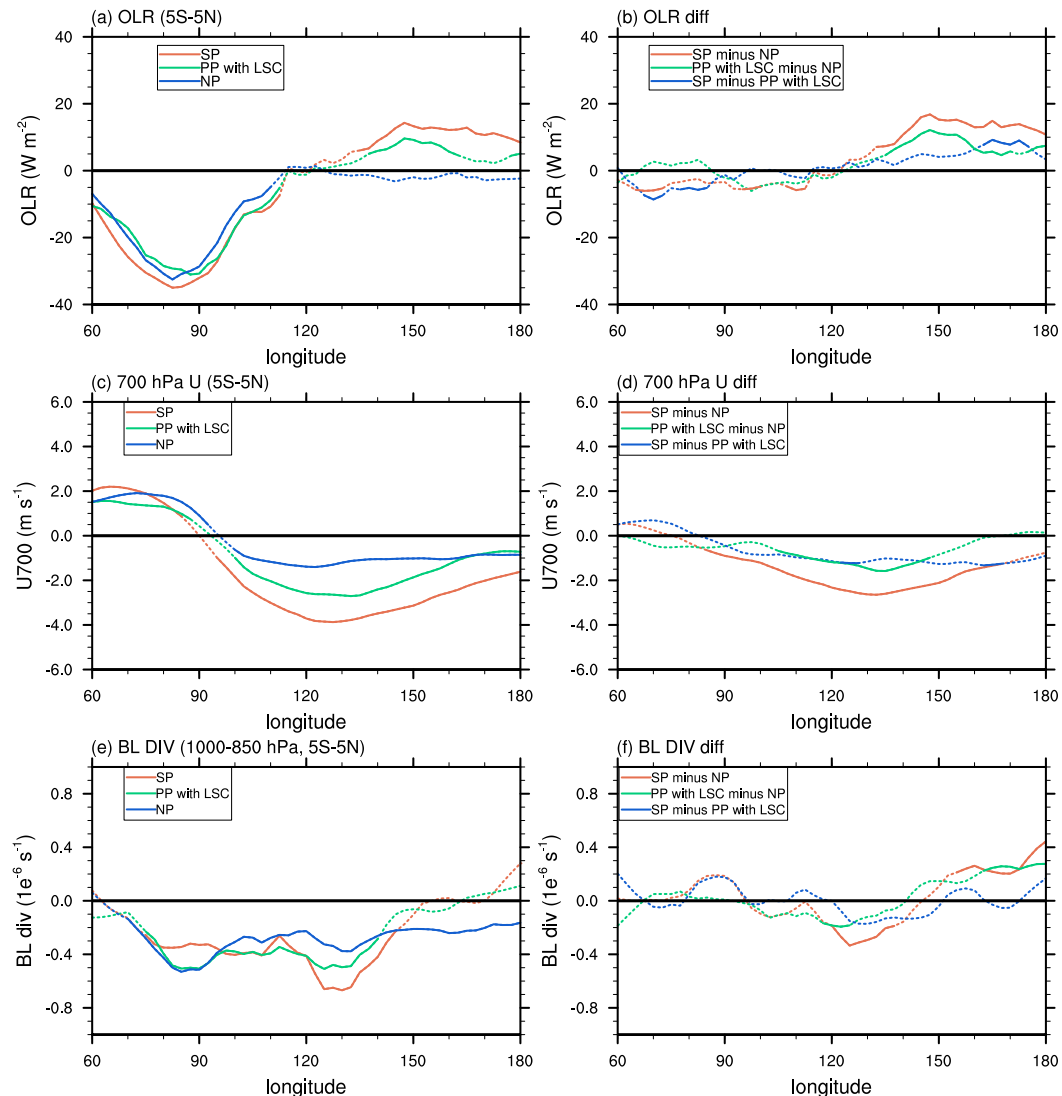
FIG. 8. (a),(c),(e) Comparison of the OLR (W m^{-2}), 700-hPa zonal wind (m s^{-1}), and BL averaged (1000–850 hPa) horizontal divergence (1×10^{-6} s^{-1}) for the three MJO groups (SP, PP with LSC, and NP) on P0, and (b),(d),(f) the differences of these fields among the three MJO groups. The solid lines indicate those values above the 95% confidence level. For the composited mean, a two-sided Student's t test is applied for statistical test. For the differences of the composited mean, a one-sided Student's t test is applied. A zonal five-point running average has been applied to the divergence field.

The leading BL convergence and the associated premoistening process could trigger congestus convection. Figure 10 shows the anomalous moisture sinks, which to some extent represent the condensational heating anomalies. It shows that there are low-level (around 900–500 hPa) condensational heating anomalies corresponding to the leading BL convergence on P0, suggesting congestus convection anomalies developing to the east of the deep convection. Once the congestus convection is triggered, the released condensational heating would further enhance the low-level vertical motion, which is manifested by the

significant low-level upward motion anomalies (105°–140°E) on P0 (Fig. 5).

To further examine how the leading BL convergence premoistens the lower atmosphere and triggers congestus convection, Fig. 11 shows the vertically averaged specific humidity (1000–650 hPa) and moisture sinks (900–500 hPa), which represent the lower-atmospheric moistening and congestus heating, respectively. It shows that corresponding to stronger leading BL convergence (Figs. 8e,f, 110°–130°E), the premoistening (Figs. 11a,b, 110°–130°E) and the congestus convection (Figs. 11c,d, 110°–130°E) are stronger in the SP and PP with LSC
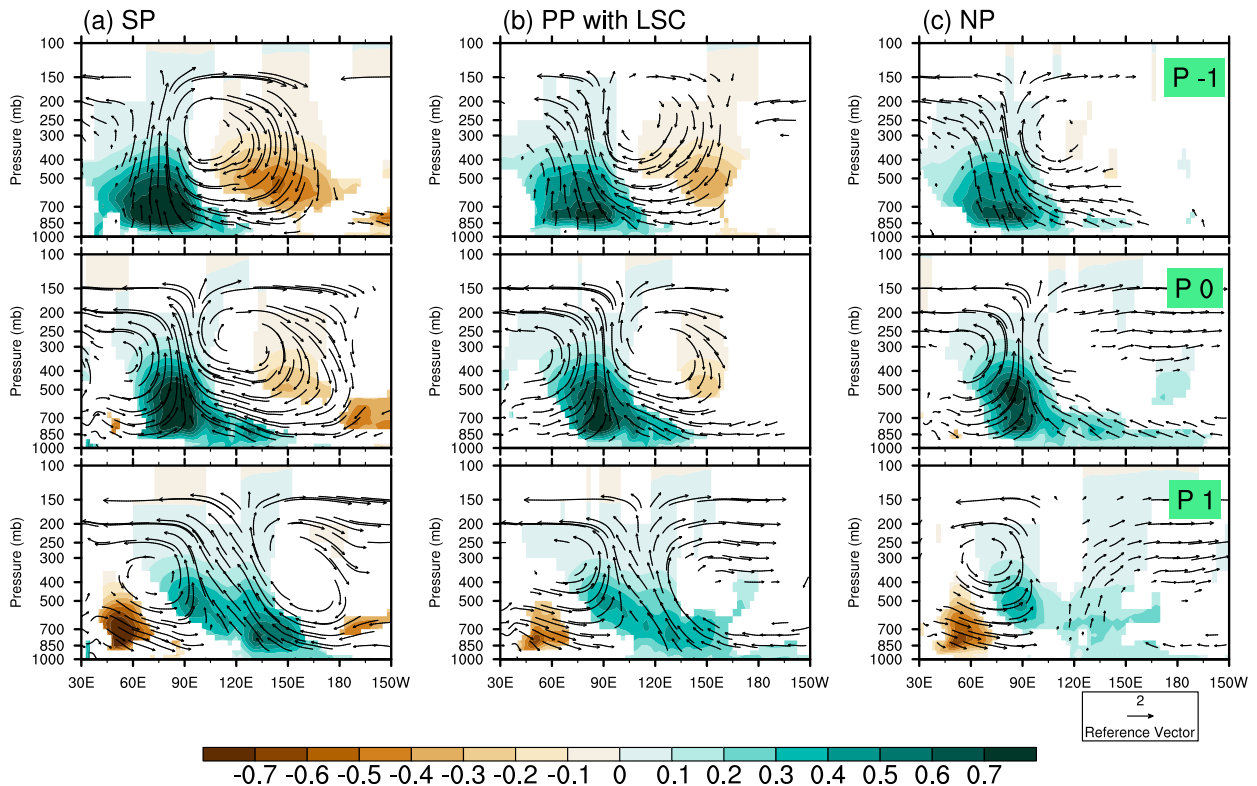
FIG. 9. As in Fig. 5, but the shadings denote the specific humidity anomalies (g kg^{-1}) averaged between 5°S and 5°N.

cases than the NP cases. The differences of the premoistening and the congestus heating between the SP cases and the NP cases are significant around 115°–130°E, while the differences between PP with LSC cases and the NP cases are significant around 110°–125°E. As a result, the enhanced leading BL convergence favors the lower-tropospheric premoistening and triggering congestus convection.

The sustained leading congestus convection by BL convergence can precondition the lower to midtroposphere (Johnson et al. 1999; Benedict and Randall 2007; Del Genio et al. 2012), favoring the transition of congestus to deep convection (Kuang and Bretherton 2006; Waite and Khouider 2010). With the FWC being coupled to the deep convection, the congestus convection anomalies deepen on $P + 1$ in the SP and the PP with LSC cases, which is manifested by the deepening of the extents of vertical velocity (Fig. 5) and the associated condensational heating (Fig. 10). These transitions from congestus to deep convection lead to eastward propagations of the MJO in the SP and PP with LSC cases. On the other hand, the decoupling of FWC from the IO deep convection leads to dissipation of the leading BL convergence on $P + 1$ in the NP cases (Fig. 7). Without the leading BL convergence, the congestus convection could not sustain and is unable to trigger new deep

convection. This is manifested by Figs. 5 and 10 that there is no new deep convection developed to the east of the existing deep convection in the NP cases on $P + 1$.

In summary, the intensified FWC enhances the leading BL convergence, which premoistens the lower atmosphere and triggers the congestus convection; the sustained congestus convection by BL convergence preconditions the lower to middle troposphere, thus favoring the transition from congestus to deep convection and leading to the eastward propagation of the MJO's deep convection. Without the coupling of the FWC, no new deep convection will develop in the absence of the BL convergence and the associated premoistening. Therefore, the coupling of the FWC to the MJO deep convection favors the eastward propagation of the MJO.

d. Comparison between PP with and without LSC cases

Although the PP without LSC cases have a very small sample size (only six cases), they suggest that LSC is a prevailing precursor but not a necessary condition for MJO propagation. Figure 12 compares the composites for the PP with and without LSC cases. Both cases have convection signals over the eastern IO region (Fig. 12a). However, over the MC (110°–140°E) the PP without
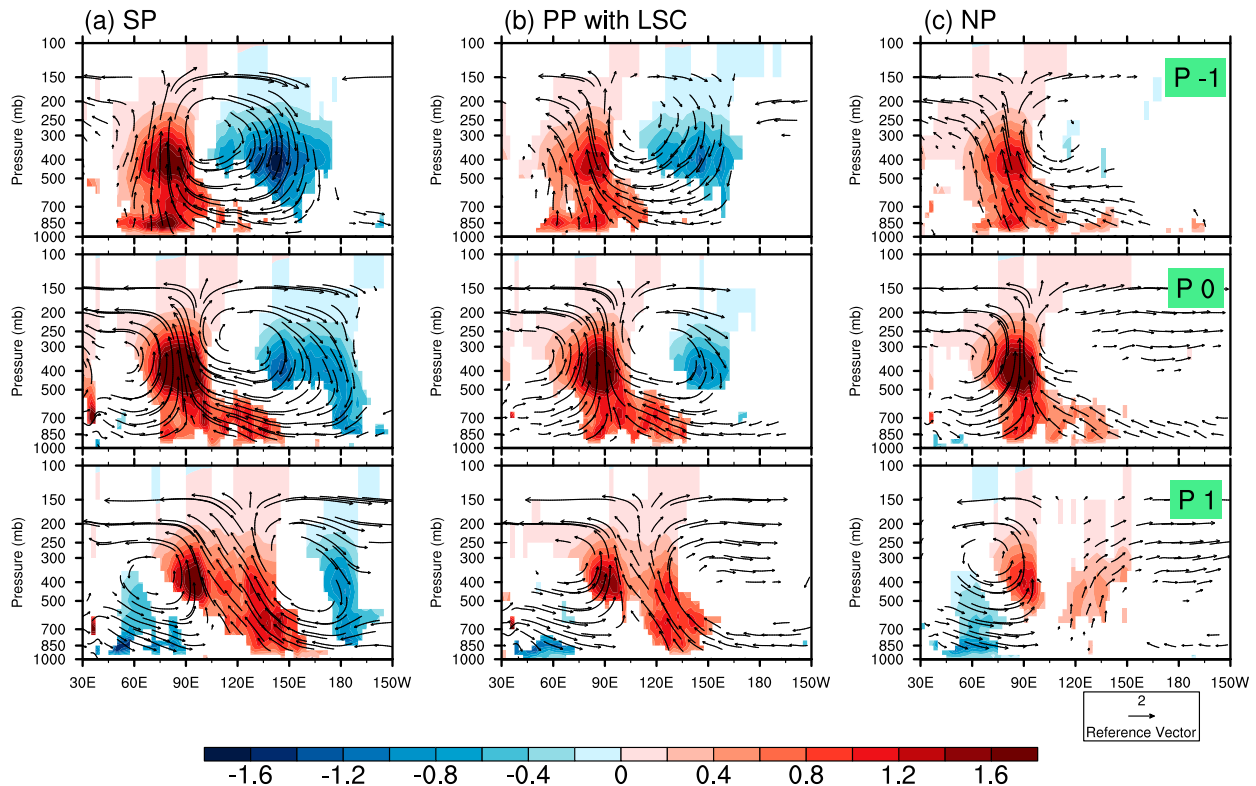
FIG. 10. As in Fig. 5, but the shadings denote the moisture sink anomalies (Q_2, 0.01 J kg^{-1} s^{-1}) averaged between 5°S and 5°N.

LSC cases show distinct negative OLR anomalies (albeit insignificant), which are accompanied by strong (significant) BL convergence (Fig. 12b) and eastward extended easterly anomalies (Fig. 12c). With the leading BL convergence, there is low-level premoistening (Fig. 12d) and low-level Q_2 (Fig. 12e) to the east of the IO deep convection, which contribute to the eastward propagation of the PP without LSC cases. It should be noted that because of the small sample size (only six cases), there is large uncertainty in the composites of PP without LSC cases, so that significant signals occur only in limited regions. Nevertheless, the PP without LSC group shows similar eastward-propagation mechanism as the other propagating MJO groups. That is, the leading BL convergence premoistens the lower troposphere and triggers the lower-tropospheric heating.

e. The dominant process for the premoistening

Since the premoistening process is critical for the eastward propagation of the MJO, an interesting question is which process dominates the premoistening process. What is more important: the vertical moisture advection or the horizontal moisture advection? To address this question, we compare the vertical structures of the intraseasonal components of the vertical $[-\omega(\partial q/\partial p)]$ and the horizontal $(-\mathbf{v} \cdot \nabla q)$ moisture

advection in Figs. 13. The intraseasonal component of the moisture advection is calculated as follows. First, the daily moisture and wind are used to calculate the horizontal and vertical moisture advection; then the data filtering described in section 2 is applied to obtain the intraseasonal component of the moisture advection. As shown in Fig. 13, there are low-level positive vertical moisture advection anomalies over 105°–140°E in the three MJO groups on P0. These low-level vertical moisture advection anomalies have similar vertical structures with the low-level moisture anomalies (Fig. 9). Additionally, the horizontal moisture advection to the east of the deep convection is much weaker than the vertical moisture advection. Thus, the premoistening of the lower atmosphere to the east of the IO deep convection is mainly attributed to the vertical moisture advection associated with the leading BL convergence and the congestus. This is consistent with previous studies (Benedict and Randall 2007; Hsu and Li 2012).

Here we get a different result from Kim et al. (2014), who found that the premoistening is attributed to the horizontal advection. The difference mainly comes from the vertical integration (1000–100 hPa) used by Kim et al. (2014). The vertical integration of vertical moisture advection will have a large cancelation between the lower and the upper levels in the region where shallow
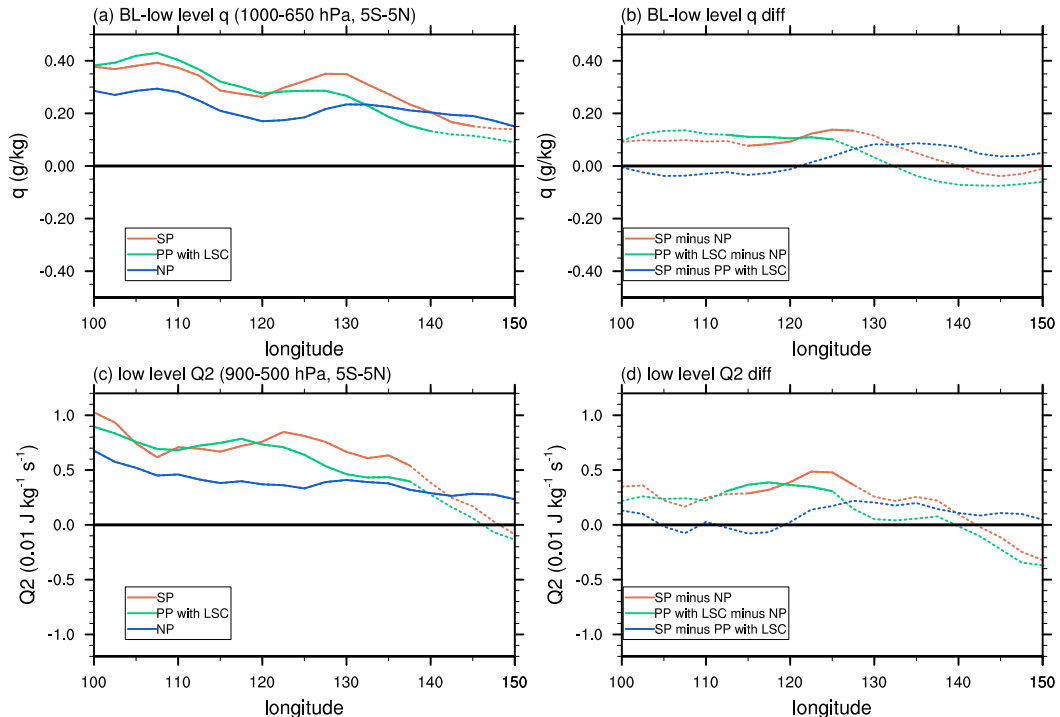
FIG. 11. (a),(c) Comparison of the BL low-level (1000–650 hPa averaged) specific humidity (g kg^{-1}) and low-level (900–500 hPa averaged) moisture sinks (0.01 J kg^{-1} s^{-1}) for the three MJO groups (SP, PP with LSC, and NP) on P0, and (b),(d) the differences of these fields among the three MJO groups. The solid lines indicate those values above the 95% confidence level. For the composited mean, a two-sided Student's t test is applied for statistical test. For the differences of the composited mean, a one-sided Student's t test is applied. A zonal three-point running average has been applied to the moisture and moisture sinks.

and congestus convection prevail. For example, the premoistening at the low levels between 110° and 140°E in the SP cases on P0 is primarily attributed to the vertical moisture advection. However, when performing vertical integration, the positive low-level vertical moisture advection will be largely canceled by the upper-level drying associated with the subsidence of the LSC. On the other hand, the vertically integrated horizontal moisture advection will have positive values to the east of the deep convection. Therefore, it may lead to the misleading impression that the horizontal moisture advection is important for the premoistening process in the SP cases.

5. Causes of the leading suppressed convection

As shown in section 4, the LSC can enhance the coupling between the deep convection and the FWC, and the FWC can promote the eastward propagation of the MJO. Thus, it is important to ask how the LSC is generated. The LSC in the SP cases comes from the eastward propagation of the preceding IO suppressed convection (Fig. 2a), while in the PP with LSC cases it does not come from the eastward propagation of the

preceding IO dry phase (Fig. 2b). Since a SP case originally starts from a PP case, it is more interesting to know the causes of the LSC in the PP with LSC cases.

To figure this out, we first examine the evolution of OLR and low-level circulation in the PP with LSC cases. As shown in Fig. 4b, prior to the onset of the IO convection, there is an IO dry phase associated with the MJO on $P - 3$. There are dry signals in the MC region (albeit insignificant to be displayed), which are potentially attributed to the leading BL divergence to the east of the IO dry phase. On $P - 2$, the IO dry phase dissipates, and the dry signals in the MC region become significant (albeit very weak), but they are not the dry phase of the MJO, as they are too weak and there is no significant associated circulation. As the IO convection is initiated on $P - 1$, the MC–WP dry signals develop into LSC and shift northward (0°–20°N, 140°–170°E). However, there are no significant circulation anomalies over the MC–WP region on $P - 2$ and $P - 1$. Thus, the low-level circulation might not explain the development of the LSC on $P - 1$, and this development of the LSC over the MC–WP region on $P - 1$ should not be interpreted as a result of eastward propagation of the
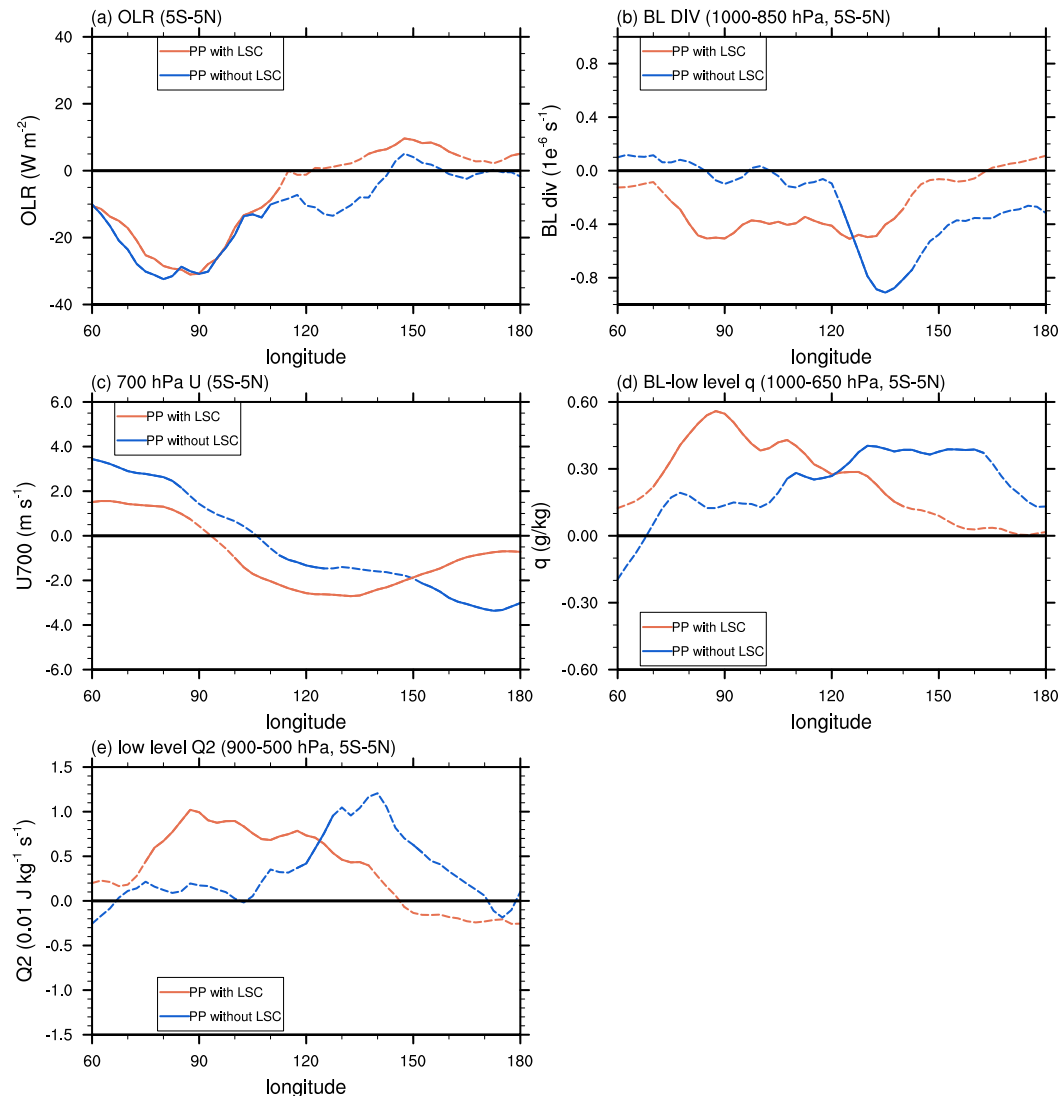
FIG. 12. Comparison of the (a) OLR (W m^{-2}), (b) BL averaged (1000–850 hPa) horizontal divergence (1×10^{-6} s^{-1}), (c) 700-hPa zonal wind (m s^{-1}), (d) BL low-level (1000–650 hPa averaged) specific humidity (g kg^{-1}), and (e) low-level (900–500 hPa averaged) moisture sinks (0.01 J kg^{-1} s^{-1}) for the PP with LSC and PP without LSC cases. The solid lines indicate those values above the 95% confidence level. A zonal five-point running average has been applied to the divergence field. A zonal three-point running average has been applied to the moisture and moisture sinks.

preceding IO dry phase like the SP cases. It is worthy to note that there are also very weak dry signals developed in WP region on $P - 2$ in the NP cases (Fig. 4c), similar to the PP with LSC cases. The difference is that these weak dry signals in the NP cases do not develop into LSC on $P - 1$. In the following argument, we will demonstrate that the upper-level circulation is responsible for the development of the LSC on $P - 1$ in the PP with LSC cases.

To study the evolution of the upper-level circulation, Fig. 14 shows the 200-hPa streamfunction anomalies, the associated WAF, and the OLR anomalies for the three

MJO groups. The basic states used for calculating the WAF are the composites of the 91-day running mean fields, and the wave components of the WAF are calculated from the circulation anomalies shown in Fig. 14. Using NDJFMA climatological basic states does not qualitatively change the WAF. For the SP cases, there is continuous propagation of suppressed convection from the IO to the WP ($P - 3$ to P0). The suppressed convection excites an anomalous cyclone to its northwest. Different from the SP cases, there is no continuous propagation of suppressed convection in the PP with LSC cases, and the evolution of the upper-level
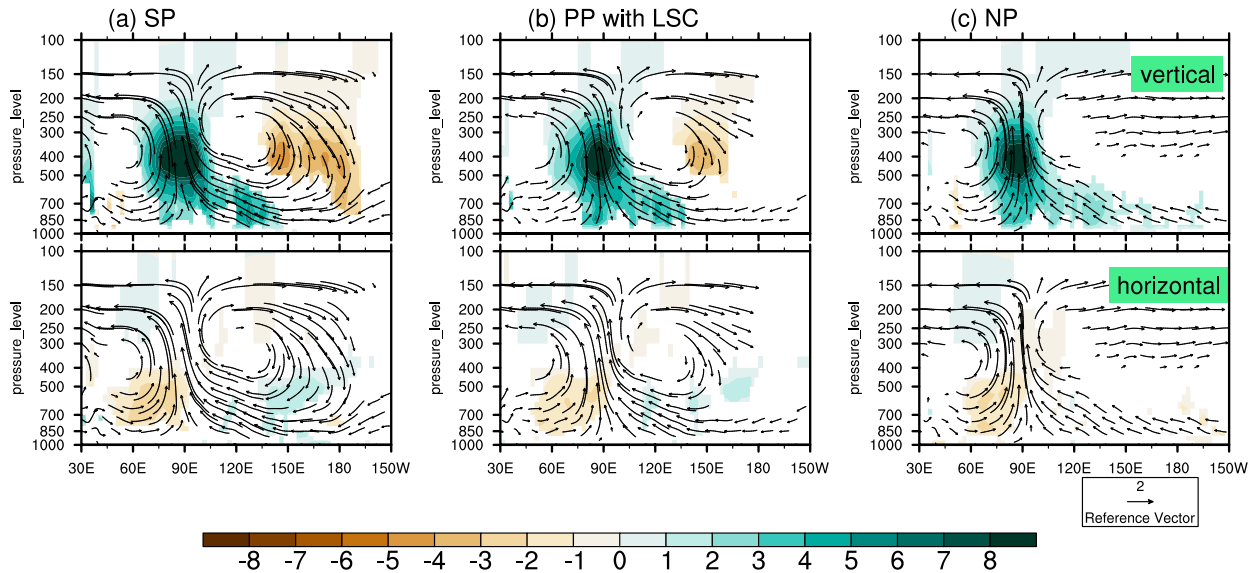
Moisture advection on P 0

FIG. 13. Comparison between the intraseasonal components of the (top) vertical $[-\omega(\partial q/\partial p)]$ and (bottom) horizontal $(-\mathbf{v} \cdot \nabla q)$ moisture advection ($1 \times 10^{-9}\,\mathrm{s}^{-1}$, shadings) averaged between 5°S and 5°N on P0 for (a) the SP cases, (b) the PP with LSC cases, and (c) the NP cases. The anomalous wind vectors over the tropical region (5°S–5°N) are also shown. Only those above the 95% confidence level are shown. For the vectors, the vertical velocity anomalies are multiplied by a factor of -100.

circulation differs. The IO suppressed convection on $P-3$ forces a western North Pacific (WNP) anticyclone (marked as ''A''), as there is eastward WAF from the IO suppressed heating region to the WNP region. On $P-2$, this anticyclone splits into an anomalous East Asia (EA) anticyclone and a central North Pacific anticyclone. There is a tropical low pressure (marked as ''L'') between these two anticyclones. Note that there is WAF converging from the EA anticyclone to this tropical low pressure, indicating the equatorward propagation of wave activity. As the convergence of WAF is enhanced on $P-1$, the tropical low pressure intensifies and shifts northward, forming an anomalous WNP cyclone (marked as ''C''), whose generation is accompanied by the intensification of the MC–WP suppressed convection. For the NP cases, there is no extratropical influence on the WNP region on $P-2$. Nevertheless, a WNP cyclone also forms on $P-1$ because of the IO heating, as manifested by WAF. However, this WNP cyclone is more zonally oriented, and there is no associated intensification of suppressed convection.

The above analysis suggests that formation of the WNP cyclone is responsible for the intensification of the MC–WP suppressed convection on $P-1$ in the PP with LSC cases. To study how this WNP cyclone affects the MC–WP suppressed convection, Fig. 15 further shows the upper-level horizontal divergence (shading) on $P-1$ for the three MJO groups. For the SP cases (Fig. 15a),

the meridional wind anomalies that converge into the MC–WP region are forced by the suppressed convection over there, which is implied by the evolution of the circulation and the associated suppressed convection (Fig. 14). For the PP with LSC cases, the northeast–southwest orientation of the WNP cyclone induces strong meridional wind to its western flank and weak zonal wind to its southern flank. This leads to significant upper-level meridional convergence anomalies over the MC–WP region (0°–20°N, 130°–170°E). Since the tropical forcing does not force the Rossby wave gyre to its east (Gill 1980), it is this WNP cyclone that strengthens the LSC by forcing the MC–WP upper-level convergence anomalies. For the NP cases, there are no significant convergence anomalies over the MC–WP region (0°–20°N, 130°–170°E) on $P-1$. The zonally oriented WNP cyclone in the NP cases could not induce strong upper-level convergence anomalies over the MC–WP region. There are only weak convergence anomalies around 130°E, which are possibly attributed to the compensating subsidence of the IO convection. Without strong upper-level convergence anomalies, no significant LSC is developed in the NP cases (Fig. 14).

Note that there is WAF converging from the IO region to the WNP cyclone on P0 in all three MJO groups (Fig. 14), which indicates the influence of IO heating on the WNP cyclone. This influence of the IO heating can be attributed to the IO heating-induced Rossby wave
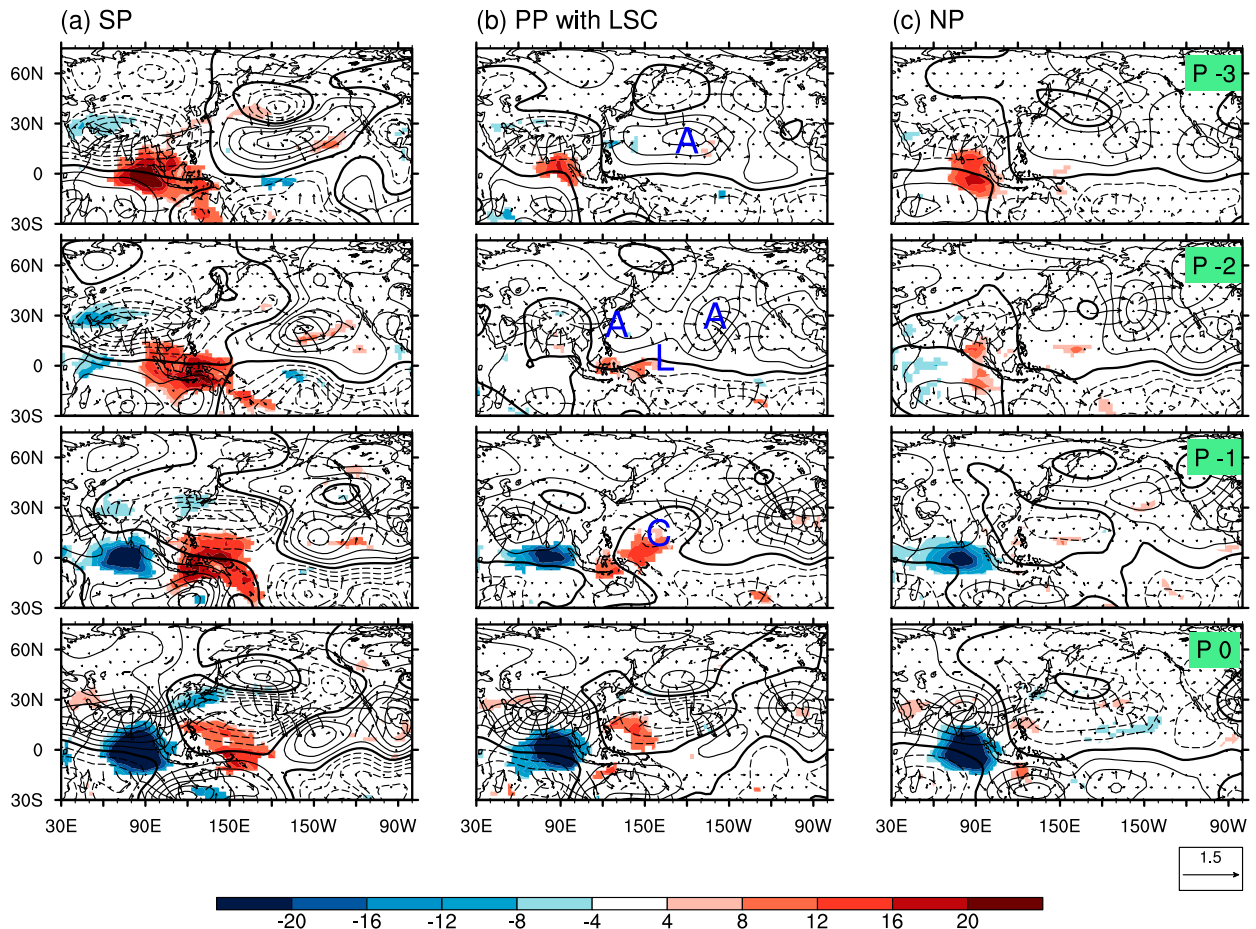
FIG. 14. Comparison of convection anomalies and upper-level circulation anomalies among the three MJO groups: composites of OLR anomalies (W m^{-2}, shadings), 200-hPa streamfunction anomalies (m^2 s^{-1}, contours), and the associated wave activity flux (m^2 s^{-2}, vectors) for (a) the SP cases, (b) the PP with LSC cases, and (c) the NP cases. The thin solid(dashed) contour indicates positive (negative) contour, and the thick solid contour indicates the zero contour. The OLR anomalies are shown for those above 95% confidence level. The contour interval is 1.5×10^6 m^2 s^{-1}.

train in the presence of basic flow (Monteiro et al. 2014). Thus, the development of the IO convection may help to maintain the already existing LSC in the SP cases and the PP with LSC cases, since it enhances the interaction between the circulation and the LSC. However, this effect alone could not force sufficiently strong suppressed convection, as manifested in the NP cases.

In conclusion, the development of the LSC over the MC–WP region in the PP with LSC cases is mainly caused by the influence of the tropical–extratropical teleconnection: the preceding IO suppressed convection forces a tropical–extratropical teleconnection, which evolves and later forms a WNP cyclone when the IO convection is initiated; this WNP cyclone generates upper-level convergence and induces significant LSC. The above process indicates a two-way interaction between the MJO's tropical heating and the associated tropical–extratropical teleconnection, as envisaged by

Lau and Phillips (1986). This two-way interaction enhances LSC and the associated FWC.

6. Conclusions and discussion

This study has investigated the causes of eastward propagation of the MJO from the IO into the WP. It is found that the eastward propagation of the MJO's convection across the MC in the boreal winter season (NDJFMA) is largely signified by the MC–WP LSC. About 88% of the propagating MJO cases are accompanied by the MC–WP LSC when the MJO's convection develops in the IO. The presence of the MC–WP LSC provides a descending branch of the FWC, of which the ascending branch is coupled to the IO deep convection.

The mechanisms of how the LSC affects the FWC and how the FWC affects the eastward propagation of the MJO are illustrated in Fig. 16. As demonstrated in
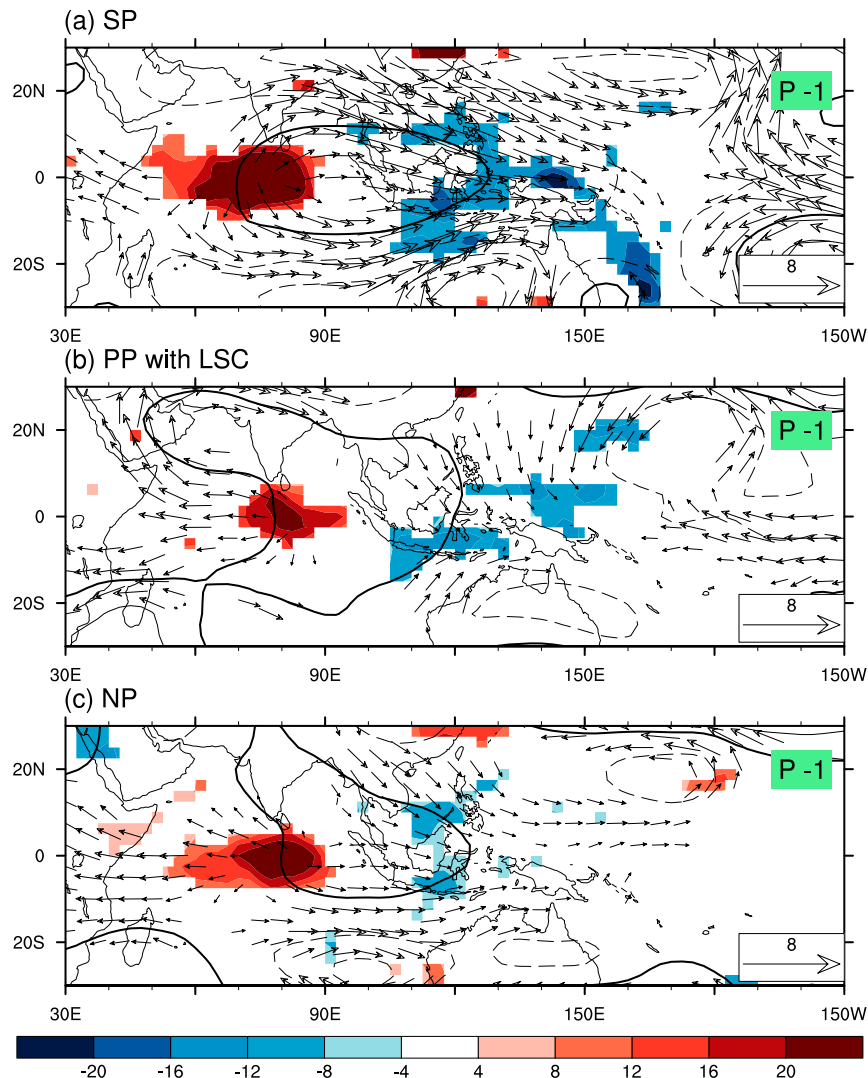
FIG. 15. Comparison of 200-hPa horizontal divergence anomalies and the associated upper-level circulation anomalies among the three MJO groups on $P - 1$: composites of 200-hPa divergence anomalies ($1 \times 10^{-7} \, \text{s}^{-1}$, shadings), geopotential height anomalies (m, contours) and anomalous wind vectors (m s^{-1}, vectors) for (a) the SP cases, (b) the PP with LSC cases, and (c) the NP cases. The divergence anomalies and the anomalous wind vectors are shown for those above the 95% confidence level. The contour interval is 10 m.

section 4, the presence of the LSC increases the differential heating between the LSC and the MJO major convection, which enhances the FWC, including both the low-level easterly anomalies and the anomalous descending motions to the east of the MJO convection. The strengthened low-level equatorial easterly (and low pressure) anomalies reinforce the leading BL convergence, which premoistens the lower troposphere and triggers more active shallow and congestus clouds. The sustained congestus convection preconditions the lower to middle troposphere, promoting the transition from congestus to deep convection, thereby leading to the eastward propagation of the MJO. Without the coupling of the FWC to the deep convection, there is no leading BL convergence and the congestus convection cannot sustain. Consequently, there is no sustained preconditioning of the lower to middle atmosphere, which impedes the development of the new deep convection. As a result, the coupling of the FWC to the deep convection can promote the eastward propagation of the MJO's deep convection.

It is noteworthy that the longitudes of significant differences in BL convergence are limited (Fig. 8f), suggesting that the strength of the BL convergence is not
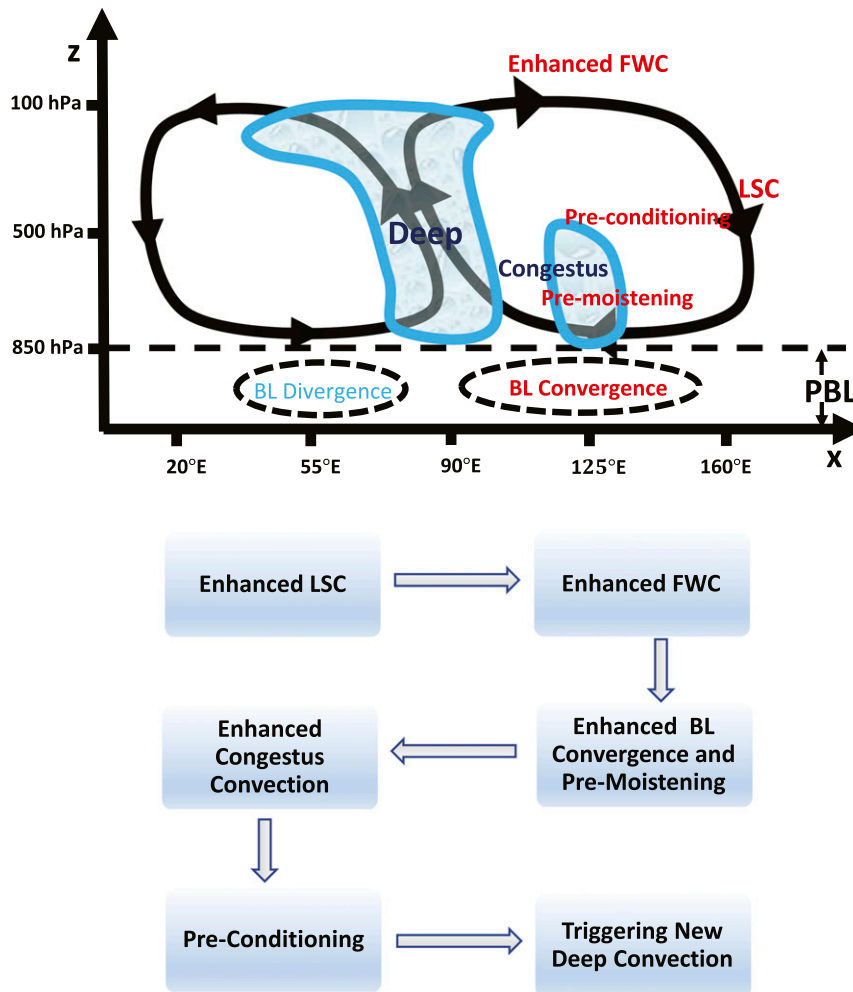
FIG. 16. Schematic diagram showing the mechanisms of how LSC affects the FWC and how the FWC affects the eastward propagation of the MJO.

solely controlled by the low-level zonal easterly (or low pressure) anomalies (which has wider longitudes of significant differences, e.g., Fig. 8d). The BL convergence intensity could also be affected by other factors (e.g., SST) (Hsu and Li 2012). It is also noteworthy that although the longitudes of significant differences in the BL convergence are limited, they play a critical role in premoistening and triggering shallow and congestus convection, as manifested in Figs. 8–12.

This study further reveals that the LSC over the MC–WP region has two major origins: one comes from the eastward propagation of the preceding IO dry phase associated with the MJO (SP cases), and the other develops concurrently when the IO convection initiates (PP with LSC cases). In the latter group the development of the LSC is caused by a two-way interaction between the MJO's tropical heating and the associated tropical–extratropical teleconnection: the preceding IO

suppressed convection forces a tropical–extratropical teleconnection, which evolves and later forms an upper-level WNP cyclone when the IO convection is initiated; the WNP cyclone generates upper-level convergence and induces significant MC–WP LSC. The result of this two-way interaction in the PP with LSC cases enhances the LSC and the associated FWC.

Although we focus on the eastward propagation of active convection in this study, the proposed mechanism also applies to the suppressed convection, as implied in Fig. 2. An important feature of Fig. 2 is that the eastward propagation of active convection is followed by well-organized eastward propagation of suppressed convection (Figs. 2a and 2b), while the nonpropagating active convection is followed by the nonpropagating suppressed convection (Fig. 2c). This is also true in Fig. 3. This suggests that the leading MC–WP active convection also favors the eastward propagation of IO suppressed

convection. The mechanism is similar: the leading MC–WP active convection affects the coupling of the reversed FWC to the IO suppressed deep convection.

The MC is known for exerting a "barrier effect" on the MJO's eastward propagation (Rui and Wang 1990; Hendon and Salby 1994; Hsu and Lee 2005; Zhang and Ling 2017). The present study provides a mechanism for the MJO to propagate across the MC region, which can be related to the previous studies. Zhang and Ling (2017) have showed that MJO events could not propagate through the MC when their convection over the land in the MC dominates that over the sea, while Hagos et al. (2016) have demonstrated that the diurnal cycle over the MC can enhance the stationary convection over land, which prevents MJO's eastward propagation. Zhang and Ling (2017) have suggested that damping the diurnal forcing may help overcome the barrier effect. The propagation mechanism proposed in the present study can potentially suppress the diurnal cycle: the LSC intensifies the FWC, which enhances the premoistening of the lower atmosphere over the MC region; the enhanced premoistening and the associated congestus convection could potentially damp the diurnal cycle over land, thus favoring the propagation of the MJO across the MC region.

Since many of the state-of-the-art GCMs have difficulties in realistic simulating the MJO (Jiang et al. 2015; Ahn et al. 2017), it is interesting to ask to what degree the FWC mechanism proposed in the present study is captured by the models. This requires further analysis of the GCM output that have participated in MJO Task Force (MJOTF)/GEWEX Atmosphere System Study (GASS) Global Model Evaluation Project, so as to see whether LSC is a prevailing precursor for the eastward propagation of the simulated MJO and how the LSC is formed in the model.

The present study shows that there is a two-way interaction between the tropical–extratropical teleconnection and the MJO's tropical heating in the PP with LSC cases, which ultimately promotes the eastward propagation of the MJO's deep convection by enhancing the LSC and the associated FWC. In the NP cases, there is no such two-way interaction. However, it is unclear on what conditions this two-way interaction will occur and why it does not appear in the NP cases. To answer these questions, further studies are needed.

REFERENCES

Ahn, M.-S., D. Kim, K. R. Sperber, I.-S. Kang, E. Maloney, D. Waliser, and H. Hendon, 2017: MJO simulation in CMIP5 climate models: MJO skill metrics and process-oriented diagnosis. *Climate Dyn.*, **49**, 4023–4045, https://doi.org/10.1007/s00382-017-3558-4

Benedict, J. J., and D. A. Randall, 2007: Observed characteristics of the MJO relative to maximum rainfall. *J. Atmos. Sci.*, **64**, 2332–2354, https://doi.org/10.1175/JAS3968.1.

Dee, D., and Coauthors, 2011: The ERA-Interim reanalysis: Configuration and performance of the data assimilation system. *Quart. J. Roy. Meteor. Soc.*, **137**, 553–597, https://doi.org/10.1002/qj.828.

Del Genio, A. D., Y. Chen, D. Kim, and M.-S. Yao, 2012: The MJO transition from shallow to deep convection in *CloudSat*/CALIPSO data and GISS GCM simulations. *J. Climate*, **25**, 3755–3770, https://doi.org/10.1175/JCLI-D-11-00384.1.

Duchon, C. E., 1979: Lanczos filtering in one and two dimensions. *J. Appl. Meteor.*, **18**, 1016–1022, https://doi.org/10.1175/1520-0450(1979)018<1016:LFIOAT>2.0.CO;2.

Feng, J., T. Li, and W. Zhu, 2015: Propagating and nonpropagating MJO events over Maritime Continent. *J. Climate*, **28**, 8430–8449, https://doi.org/10.1175/JCLI-D-15-0085.1.

Gill, A. E., 1980: Some simple solutions for heat-induced tropical circulation. *Quart. J. Roy. Meteor. Soc.*, **106**, 447–462, https://doi.org/10.1002/qj.49710644905.

Hagos, S. M., C. Zhang, Z. Feng, C. D. Burleyson, C. De Mott, B. Kerns, J. J. Benedict, and M. N. Martini, 2016: The impact of the diurnal cycle on the propagation of Madden-Julian Oscillation convection across the Maritime Continent. *J. Adv. Model. Earth Syst.*, **8**, 1552–1564, https://doi.org/10.1002/2016MS000725.

Hendon, H. H., and M. L. Salby, 1994: The life cycle of the Madden–Julian oscillation. *J. Atmos. Sci.*, **51**, 2225–2237, https://doi.org/10.1175/1520-0469(1994)051<2225:TLCOTM>2.0.CO;2.

Hsu, H.-H., and M.-Y. Lee, 2005: Topographic effects on the eastward propagation and initiation of the Madden–Julian oscillation. *J. Climate*, **18**, 795–809, https://doi.org/10.1175/JCLI-3292.1.

Hsu, P.-c., and T. Li, 2012: Role of the boundary layer moisture asymmetry in causing the eastward propagation of the Madden–Julian oscillation. *J. Climate*, **25**, 4914–4931, https://doi.org/10.1175/JCLI-D-11-00310.1.

Jiang, X., and Coauthors, 2015: Vertical structure and physical processes of the Madden-Julian oscillation: Exploring key model physics in climate simulations. *J. Geophys. Res. Atmos.*, **120**, 4718–4748, https://doi.org/10.1002/2014JD022375.

Johnson, R. H., T. M. Rickenbach, S. A. Rutledge, P. E. Ciesielski, and W. H. Schubert, 1999: Trimodal characteristics of tropical

convection. *J. Climate*, **12**, 2397–2418, https://doi.org/10.1175/1520-0442(1999)012<2397:TCOTC>2.0.CO;2.

Kiladis, G. N., K. H. Straub, and P. T. Haertel, 2005: Zonal and vertical structure of the Madden-Julian oscillation. *J. Atmos. Sci.*, **62**, 2790–2809, https://doi.org/10.1175/JAS3520.1.

Kim, D., J.-S. Kug, and A. H. Sobel, 2014: Propagating versus nonpropagating Madden–Julian oscillation events. *J. Climate*, **27**, 111–125, https://doi.org/10.1175/JCLI-D-13-00084.1.

Kuang, Z., 2008a: Modeling the interaction between cumulus convection and linear gravity waves using a limited-domain cloud system–resolving model. *J. Atmos. Sci.*, **65**, 576–591, https://doi.org/10.1175/2007JAS2399.1.

——, 2008b: A moisture-stratiform instability for convectively coupled waves. *J. Atmos. Sci.*, **65**, 834–854, https://doi.org/10.1175/2007JAS2444.1.

——, and C. S. Bretherton, 2006: A mass-flux scheme view of a high-resolution simulation of a transition from shallow to deep cumulus convection. *J. Atmos. Sci.*, **63**, 1895–1909, https://doi.org/10.1175/JAS3723.1.

Lau, K.-M., and T. J. Phillips, 1986: Coherent fluctuations of extratropical geopotential height and tropical convection in intraseasonal time scales. *J. Atmos. Sci.*, **43**, 1164–1181, https://doi.org/10.1175/1520-0469(1986)043<1164:CFOFGH>2.0.CO;2.

Lee, S.-S., B. Wang, D. E. Waliser, J. M. Neena, and J.-Y. Lee, 2015: Predictability and prediction skill of the boreal summer intraseasonal oscillation in the Intraseasonal Variability Hindcast Experiment. *Climate Dyn.*, **45**, 2123–2135, https://doi.org/10.1007/s00382-014-2461-5.

Liebmann, B., and C. Smith, 1996: Description of a complete (interpolated) outgoing longwave radiation dataset. *Bull. Amer. Meteor. Soc.*, **77**, 1275–1277, https://doi.org/10.1175/1520-0477-77.6.1274.

Madden, R. A., and P. R. Julian, 1971: Detection of a 40–50 day oscillation in the zonal wind in the tropical Pacific. *J. Atmos. Sci.*, **28**, 702–708, https://doi.org/10.1175/1520-0469(1971)028<0702:DOADOI>2.0.CO;2.

——, and ——, 1972: Description of global-scale circulation cells in the tropics with a 40–50 day period. *J. Atmos. Sci.*, **29**, 1109–1123, https://doi.org/10.1175/1520-0469(1972)029<1109:DOGSCC>2.0.CO;2.

——, and ——, 1994: Observations of the 40–50-day tropical oscillation—A review. *Mon. Wea. Rev.*, **122**, 814–837, https://doi.org/10.1175/1520-0493(1994)122<0814:OOTDTO>2.0.CO;2.

Matthews, A. J., 2008: Primary and successive events in the Madden–Julian oscillation. *Quart. J. Roy. Meteor. Soc.*, **134**, 439–453, https://doi.org/10.1002/qj.224.

Monteiro, J. M., Á. F. Adames, J. M. Wallace, and J. S. Sukhatme, 2014: Interpreting the upper level structure of the Madden-Julian oscillation. *Geophys. Res. Lett.*, **41**, 9158–9165, https://doi.org/10.1002/2014GL062518.

Neena, J. M., J. Y. Lee, D. Waliser, B. Wang, and X. Jiang, 2014: Predictability of the Madden–Julian oscillation in the Intraseasonal Variability Hindcast Experiment (ISVHE). *J. Climate*, **27**, 4531–4543, https://doi.org/10.1175/JCLI-D-13-00624.1.

Rui, H., and B. Wang, 1990: Development characteristics and dynamic structure of tropical intraseasonal convection anomalies. *J. Atmos. Sci.*, **47**, 357–379, https://doi.org/10.1175/1520-0469(1990)047<0357:DCADSO>2.0.CO;2.

Takaya, K., and H. Nakamura, 2001: A formulation of a phase-independent wave-activity flux for stationary and migratory quasigeostrophic eddies on a zonally varying basic flow. *J. Atmos. Sci.*, **58**, 608–627, https://doi.org/10.1175/1520-0469(2001)058<0608:AFOAPI>2.0.CO;2.

Waite, M. L., and B. Khouider, 2010: The deepening of tropical convection by congestus preconditioning. *J. Atmos. Sci.*, **67**, 2601–2615, https://doi.org/10.1175/2010JAS3357.1.

Wang, B., and H. Rui, 1990a: Dynamics of the coupled moist Kelvin–Rossby wave on an equatorial β-plane. *J. Atmos. Sci.*, **47**, 397–413, https://doi.org/10.1175/1520-0469(1990)047<0397:DOTCMK>2.0.CO;2.

——, and ——, 1990b: Synoptic climatology of transient tropical intraseasonal convection anomalies: 1975–1985. *Meteor. Atmos. Phys.*, **44**, 43–61, https://doi.org/10.1007/BF01026810.

——, and T. Li, 1994: Convective interaction with boundary-layer dynamics in the development of a tropical intraseasonal system. *J. Atmos. Sci.*, **51**, 1386–1400, https://doi.org/10.1175/1520-0469(1994)051<1386:CIWBLD>2.0.CO;2.

——, and S.-S. Lee, 2017: MJO propagation shaped by zonal asymmetric structures: Results from 24 GCM simulations. *J. Climate*, **30**, 7933–7952, https://doi.org/10.1175/JCLI-D-16-0873.1.

——, and Coauthors, 2018: Dynamics-oriented diagnostics for the Madden–Julian oscillation. *J. Climate*, **31**, 3117–3135, https://doi.org/10.1175/JCLI-D-17-0332.1.

Wang, L., T. Li, E. Maloney, and B. Wang, 2017: Fundamental causes of propagating and nonpropagating MJOs in MJOTF/GASS models. *J. Climate*, **30**, 3743–3769, https://doi.org/10.1175/JCLI-D-16-0765.1.

Wheeler, M. C., and H. H. Hendon, 2004: An all-season real-time multivariate MJO index: Development of an index for monitoring and prediction. *Mon. Wea. Rev.*, **132**, 1917–1932, https://doi.org/10.1175/1520-0493(2004)132<1917:AARMMI>2.0.CO;2.

Zhang, C., 2005: Madden–Julian Oscillation. *Rev. Geophys.*, **43**, RG2003, https://doi.org/10.1029/2004RG000158.

——, 2013: Madden–Julian Oscillation: Bridging weather and climate. *Bull. Amer. Meteor. Soc.*, **94**, 1849–1870, https://doi.org/10.1175/BAMS-D-12-00026.1.

——, and J. Ling, 2017: Barrier effect of the Indo-Pacific Maritime Continent on the MJO: Perspectives from tracking MJO precipitation. *J. Climate*, **30**, 3439–3459, https://doi.org/10.1175/JCLI-D-16-0614.1.